

# Highly Homogeneous 2D/3D Heterojunction Diodes by Pulsed Laser Deposition of MoS<sub>2</sub> on Ion Implantation Doped 4H-SiC

Filippo Giannazzo,\* Salvatore Ethan Panasci, Emanuela Schilirò, Patrick Fiorenza, Giuseppe Greco, Fabrizio Roccaforte, Marco Cannas, Simonpietro Agnello, Antal Koos, Béla Pécz, Marianna Španková, and Štefan Chromik

In this paper, 2D/3D heterojunction diodes have been fabricated by pulsed laser deposition (PLD) of MoS<sub>2</sub> on 4H-SiC(0001) surfaces with different doping levels, i.e., n<sup>-</sup> epitaxial doping ( $\approx 10^{16} \text{ cm}^{-3}$ ) and n<sup>+</sup> ion implantation doping ( $> 10^{19} \text{ cm}^{-3}$ ). After assessing the excellent thickness uniformity ( $\approx 3\text{-L-MoS}_2$ ) and conformal coverage of the PLD-grown films by Raman mapping and transmission electron microscopy, the current injection across the heterojunctions is investigated by temperature-dependent current–voltage characterization of the diodes and by nanoscale current mapping with conductive atomic force microscopy. A wide tunability of the transport properties is shown by the SiC surface doping, with highly rectifying behavior for the MoS<sub>2</sub>/n<sup>-</sup> SiC junction and a strongly enhanced current injection for MoS<sub>2</sub>/n<sup>+</sup> SiC one. Thermionic emission is found the dominant mechanism ruling forward current in MoS<sub>2</sub>/n<sup>-</sup> SiC diodes, with an effective barrier  $\Phi_B = (1.04 \pm 0.09) \text{ eV}$ . Instead, the significantly lower effective barrier  $\Phi_B = (0.31 \pm 0.01) \text{ eV}$  and a temperature-dependent ideality factor for MoS<sub>2</sub>/n<sup>+</sup> SiC junctions is explained by thermionic-field-emission through the thin depletion region of n<sup>+</sup> doped SiC. The scalability of PLD MoS<sub>2</sub> deposition and the electronic transport tunability by implantation doping of SiC represents key steps for industrial development of MoS<sub>2</sub>/SiC devices.

such as the thickness-dependent bandgap, which are attractive for ultra-scaled digital electronics beyond silicon, optoelectronics, and energy applications.<sup>[1]</sup> The dangling-bond free structure of TMDs offers the unique possibility of realizing high-quality van der Waals heterostructures with bulk semiconductors for the implementation of advanced heterojunction devices exploiting current transport at the interface.<sup>[2–5]</sup> In particular, the integration of single or few layers MoS<sub>2</sub> with wide bandgap semiconductors, such as the group-III Nitrides (GaN, AlN, and AlGaIn alloys) and 4H-SiC, is currently the object of increasing interest in optoelectronics (e.g., for the realization of high responsivity dual-band photodetectors covering the spectral ranges of visible and ultraviolet),<sup>[6–11]</sup> and in electronics (e.g., for the realization of heterojunction diodes, including band-to-band tunnel diodes).<sup>[12–17]</sup>

Motivated by these interests, different approaches have been employed to fabricate such heterojunction devices,


including the transfer of MoS<sub>2</sub> flakes exfoliated from bulk crystals<sup>[6,9,10]</sup> or grown on foreign substrates,<sup>[12,13,18]</sup> and the direct deposition of MoS<sub>2</sub> on GaN<sup>[14–16]</sup> or 4H-SiC.<sup>[11,17]</sup> In particular, nearly unstrained and highly oriented monolayer MoS<sub>2</sub> triangular domains on the GaN(0001) basal plane have been

## 1. Introduction

Layered transition metal dichalcogenides (TMDs), including MoS<sub>2</sub>, WS<sub>2</sub>, MoSe<sub>2</sub>, WSe<sub>2</sub>, have been widely investigated in the last years, due to their interesting semiconducting properties,

F. Giannazzo, S. E. Panasci, E. Schilirò, P. Fiorenza, G. Greco, F. Roccaforte, S. Agnello  
CNR-IMM  
Strada VIII, Catania 5 95121, Italy  
E-mail: filippo.giannazzo@imm.cnr.it

S. E. Panasci  
Department of Physics and Astronomy  
University of Catania  
Via Santa Sofia 64, Catania 95123, Italy

 The ORCID identification number(s) for the author(s) of this article can be found under <https://doi.org/10.1002/admi.202201502>.

© 2022 The Authors. Advanced Materials Interfaces published by Wiley-VCH GmbH. This is an open access article under the terms of the Creative Commons Attribution License, which permits use, distribution and reproduction in any medium, provided the original work is properly cited.

M. Cannas, S. Agnello  
Department of Physics and Chemistry Emilio Segrè  
University of Palermo  
Via Archirafi 36, Palermo 90143, Italy

S. Agnello  
AtenCenter  
University of Palermo  
Viale delle Scienze Ed.18, Palermo 90128, Italy

A. Koos, B. Pécz  
Centre for Energy Research  
Institute of Technical Physics and Materials Science  
Konkoly-Thege ut 29–33, Budapest 1121, Hungary

M. Španková, Š. Chromik  
Institute of Electrical Engineering SAS  
Dúbravská cesta 9, Bratislava 84104, Slovakia

DOI: 10.1002/admi.202201502

obtained by chemical vapor deposition (CVD) at a temperature of 700–800 °C.<sup>[14,19,20]</sup> Epitaxial MoS<sub>2</sub> growth on GaN has been also obtained by the pulsed laser deposition (PLD) technique.<sup>[21]</sup> The high-quality epitaxial growth has been ascribed to the very low (<1%) in-plane lattice mismatch between the MoS<sub>2</sub> and GaN hexagonal lattices, and to the similar thermal expansion coefficients of the two materials.

On the other hand, the larger lattice constants mismatch ( $\approx 2.9\%$ , with  $a_{\text{MoS}_2} = 3.162 \text{ \AA}$  and  $a_{4\text{H-SiC}} = 3.073 \text{ \AA}$ )<sup>[22]</sup> and the difference in thermal expansion coefficients ( $\alpha_{\text{MoS}_2} = 1.90 \times 10^{-6} \text{ K}^{-1}$ ,  $\alpha_{4\text{H-SiC}} = 4.47 \times 10^{-6} \text{ K}^{-1}$ )<sup>[23,24]</sup> between MoS<sub>2</sub> and 4H-SiC may contribute to interfacial strain. To date, few layers or monolayer MoS<sub>2</sub> films uniformly covering the SiC(0001) surface have been reported by CVD approaches, i.e., the single-step CVD with vapors from S and MoO<sub>3</sub> powders<sup>[11]</sup> or the sulfurization of predeposited Mo thin films.<sup>[17]</sup> Highly crystalline few layers MoS<sub>2</sub> on 6H-SiC(0001) have been also obtained by PLD at a substrate temperature of 700 °C.<sup>[21]</sup> Furthermore, inhomogeneous MoS<sub>2</sub> flakes with dendritic shape,<sup>[25]</sup> or vertically standing triangular MoS<sub>2</sub> domains with respect to the basal planes of 6H-SiC<sup>[26]</sup> and 4H-SiC<sup>[27]</sup> have been obtained by CVD properly tailoring the growth conditions. While vertically standing MoS<sub>2</sub> exposing edges can be interesting for catalysis and hydrogen evolution reaction (HER) applications,<sup>[27]</sup> layered MoS<sub>2</sub> films uniformly covering the SiC(0001) basal plane are highly attractive as building blocks of heterojunction devices exploiting vertical current transport at MoS<sub>2</sub>/SiC interfaces. These can find application both in the state-of-the-art 4H-SiC technology (Schottky and Junction Barrier Schottky diodes) for energy-efficient power conversion,<sup>[28]</sup> as well as for the implementation of novel device concepts for ultra-fast switching, including p<sup>+</sup>-MoS<sub>2</sub>/n<sup>+</sup>-SiC Esaki diodes<sup>[29]</sup> and vertical hot electron transistors with a n-MoS<sub>2</sub> base<sup>[30,31]</sup> and n<sup>+</sup>-SiC emitter. Besides the reported studies, a more comprehensive understanding of the structural properties and of the mechanisms ruling current transport across MoS<sub>2</sub>/SiC interfaces is mandatory for the future development of these heterojunction devices. However, to date, only a few studies reported on the electronic transport in MoS<sub>2</sub>/SiC diodes, mainly focused on anisotype (p/n) junctions of p<sup>+</sup> MoS<sub>2</sub> with n<sup>+</sup> 4H-SiC,<sup>[12,29]</sup> whereas there is a lack of knowledge on the isotype (n/n) MoS<sub>2</sub>/4H-SiC heterojunctions.

In this paper, the PLD technique has been employed to deposit highly uniform  $\approx 3\text{-L-MoS}_2$  films on the surface of 4H-SiC(0001) samples with different n-type doping levels, i.e., low n-type doping ( $10^{16} \text{ cm}^{-3}$ ) epitaxy and degenerate n-type doping ( $>10^{19} \text{ cm}^{-3}$ ) by phosphorous ion implantation. After assessing the MoS<sub>2</sub> thickness uniformity and the structural properties of the heterojunction by Raman mapping combined with atomic resolution transmission electron microscopy (TEM), the electronic transport mechanisms at the interfaces have been deeply investigated both on macroscopic diodes and at nanoscale by conductive atomic force microscopy (C-AFM) current mapping.<sup>[32,33]</sup> A wide tunability of current injection at the hetero-interfaces by the near-surface doping of SiC is demonstrated, showing a highly rectifying behavior on n<sup>-</sup> 4H-SiC and strongly enhanced current injection on n<sup>+</sup>- implanted 4H-SiC. Furthermore, the mechanisms ruling current injection under forwarding bias polarization (i.e., thermionic emission above the MoS<sub>2</sub>/SiC conduction band discontinuity for n<sup>-</sup> 4H-SiC and thermionic field emission across the ultra-thin depletion region

of SiC for n<sup>+</sup> 4H-SiC) have been discussed based on the results of temperature-dependent current-voltage (I–V) characterization of diodes and C-AFM nanoscale current mapping.

## 2. Experimental Section

Two 4H-SiC(0001) samples with different n-type surface doping have been used for the MoS<sub>2</sub> PLD growth experiments. They were prepared from the same initial 4H-SiC (0001) 4°-off wafer, consisting of a n<sup>+</sup> substrate covered by a 5 μm moderately n-type doped epitaxial layer, with a carrier concentration of  $\approx 1 \times 10^{16} \text{ cm}^{-3}$  evaluated by Hg-probe capacitance measurements. The first sample (from now on named n<sup>-</sup>-SiC sample) was a 10 mm × 10 mm piece cut from this wafer. For the second sample (from now on named n<sup>+</sup>-SiC sample), phosphorous (P) ions implantation at energies from 30 to 200 keV and doses from  $7.5 \times 10^{13}$  to  $5 \times 10^{14} \text{ cm}^{-2}$  was performed at a temperature of 400 °C, followed by activation annealing at 1675 °C in Ar ambient. These implant and annealing conditions resulted in a n<sup>+</sup> doping profile, with an active donors concentration  $\approx 1 \times 10^{19} \text{ cm}^{-3}$  in the near surface region and a concentration plateau of  $\approx (8.5\text{--}9) \times 10^{19} \text{ cm}^{-3}$  in the depth range from 90 to 170 nm.<sup>[34,35]</sup> The phosphorous doping concentration profile, measured by secondary ions mass spectrometry (SIMS), and the active donor's concentration, evaluated by scanning capacitance microscopy on cross-sectioned samples, are illustrated in Figure S1, Supporting Information.<sup>[34]</sup>

Ultra-thin films of MoS<sub>2</sub> have been grown on the two different 4H-SiC samples by PLD with a MBE/PLD-2000 system equipped a 248 nm wavelength KrF excimer laser Compex 102, and using a target of MoS<sub>2</sub>. Two-inch diameter commercial stoichiometric MoS<sub>2</sub> target rotated at the speed of 6 rpm. The substrates ( $10 \times 10 \text{ mm}^2$ ) were placed on the rotating holder 10 cm away from the target. The deposition temperature was about 700 °C. After the deposition, the temperature was decreased at a rate of 50 °C min<sup>-1</sup> until 200 °C, and then by natural cooling. The KrF excimer laser operated at a 4 Hz pulse rate. The energy pulse was 60–70 mJ and the laser spot size was 2 mm<sup>2</sup>. The total number of the pulses to achieve the deposition of 3–4 L MoS<sub>2</sub> typically ranges from 330–380 pulses. The exact number depends on the state of the MoS<sub>2</sub> target at the starting of the deposition, the accuracy of pulse energy, and the substrate position on the rotating heater. A preliminary calibration was performed immediately before the deposition on the 4H-SiC substrates. Based on this calibration, a number of 380 pulses was used in this experiment to achieve the desired MoS<sub>2</sub> thickness.

The thickness uniformity of MoS<sub>2</sub> was evaluated by Raman spectroscopy and mapping on different areas of the samples, using a Horiba HR-Evolution micro-Raman system with a confocal microscope (100× objective) and a laser excitation wavelength of 532 nm. All the spectra have been calibrated using the E<sub>2</sub>(TA) vibrational peak of 4H-SiC (at 204 cm<sup>-1</sup>) as reference. Furthermore, high-resolution transmission electron microscopy (HR-TEM) and energy dispersion spectroscopy (EDS) analyses of the cross-sectioned MoS<sub>2</sub>/SiC samples (lamellas preparation with focused ion beam) were carried out with an aberration-corrected Thermofisher Themis 200 microscope. The current injection at the interface between the PLD-grown MoS<sub>2</sub> and 4H-SiC was

probed at nanoscale by conductive atomic force microscopy (C-AFM) with a DI3100 system by Bruker with Nanoscope V electronics. The sample's surface was scanned with Pt-coated Si tips (with curvature radius  $r_{\text{tip}} \approx 5$  nm) to simultaneously collect morphology and current maps, while applying a potential difference between the tip and the samples' backside. Furthermore, local  $I$ - $V$  curves were acquired on arrays of tip positions on the samples' surface. Finally, macroscopic circular contacts with 100  $\mu\text{m}$  radius were lithographically fabricated on both the  $n^-$  SiC and  $n^+$  SiC by deposition of a Ni(20 nm)/Au(80 nm) metal stack, followed by resist lift-off. Temperature-dependent  $I$ - $V$  characterization of the resulting metal/MoS<sub>2</sub>/SiC heterojunction diodes was carried out using a Karl Suss Microtec probe station equipped with a HP4156B parameter analyzer.

### 3. Results and Discussion

The as-deposited MoS<sub>2</sub> films were initially investigated by Raman mapping on different sample areas, in order to evaluate the MoS<sub>2</sub> thickness uniformity. Two representative Raman

spectra collected on the MoS<sub>2</sub>/ $n^-$ -SiC surface (blue line) and on the MoS<sub>2</sub>/ $n^+$ -SiC one (red line) are reported in **Figure 1a**. The most prominent features in the spectral range from 150 to 500  $\text{cm}^{-1}$  are represented by the  $E_2(\text{TA})$  mode at 204  $\text{cm}^{-1}$  associated to 4H-SiC substrate, and the two first-order MoS<sub>2</sub> vibrational modes ( $E_{2g}$  and  $A_{1g}$ ) between 370 and 420  $\text{cm}^{-1}$ . In particular, measuring the wavenumber difference ( $\Delta\omega = \omega_{A_{1g}} - \omega_{E_{2g}}$ ) between these two characteristic Raman peaks is commonly taken as a straightforward way to evaluate the number of MoS<sub>2</sub> layers.<sup>[36]</sup> The thickness uniformity of the PLD-grown MoS<sub>2</sub> films was determined by statistical analysis on arrays of 144 Raman spectra collected on 10  $\mu\text{m} \times 10 \mu\text{m}$  areas. Figure 1b,c shows the color maps of the  $\Delta\omega$  values extracted from the arrays measured on the MoS<sub>2</sub>/ $n^-$ -SiC and MoS<sub>2</sub>/ $n^+$ -SiC samples, respectively. The number of MoS<sub>2</sub> layers corresponding to the  $\Delta\omega$  values are also indicated in the color bar in the lowest part of Figure 1c. Furthermore, the histograms of the  $\Delta\omega$  values extracted from the two color maps are reported in Figure 1d, showing very narrow distributions with the maximum values and standard deviations of  $24.02 \pm 0.07 \text{ cm}^{-1}$  and  $23.58 \pm 0.13 \text{ cm}^{-1}$  for the MoS<sub>2</sub> on  $n^-$ -type 4H-SiC (blue histogram) and  $n^+$  4H-SiC (red histogram),

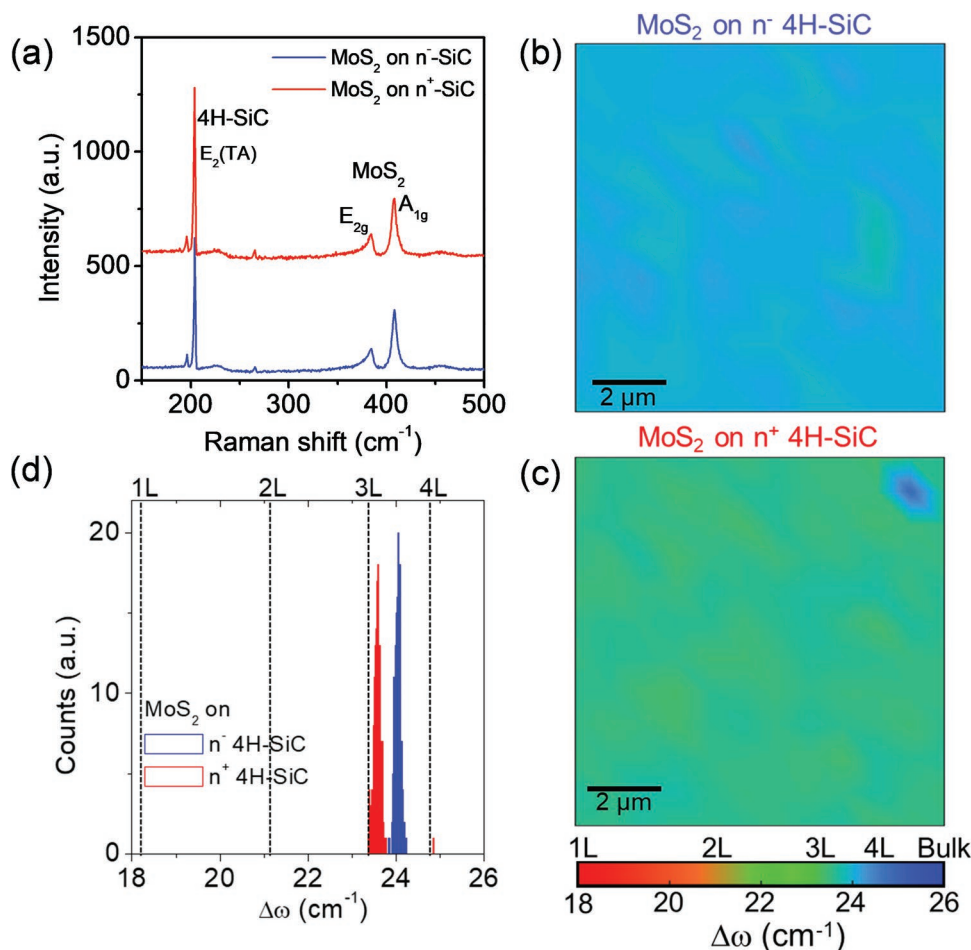


**Figure 1.** a) Typical Raman spectra of PLD grown MoS<sub>2</sub> on  $n^-$ -SiC (blue line) and on  $n^+$ -SiC (red line), showing the  $E_2(\text{TA})$  peak belonging to the 4H-SiC substrate and the two characteristics in-plane ( $E_{2g}$ ) and out-of plane ( $A_{1g}$ ) vibrational modes of MoS<sub>2</sub>. Color maps of the  $A_{1g}$  and  $E_{2g}$  wavenumber differences  $\Delta\omega = \omega_{A_{1g}} - \omega_{E_{2g}}$  evaluated from an array of 144 Raman spectra collected on 10  $\mu\text{m} \times 10 \mu\text{m}$  areas of the MoS<sub>2</sub>/ $n^-$ -SiC b) and MoS<sub>2</sub>/ $n^+$ -SiC c) samples. The number of MoS<sub>2</sub> layers associated with the  $\Delta\omega$  value is indicated in the color scale. d) Histograms of the  $\Delta\omega$  values associated with the two color maps, showing a very uniform thickness distribution (from 3 to 4 layers) of MoS<sub>2</sub> on the two samples.



respectively. These statistical analyses, performed at different positions of the two 10 mm × 10 mm samples, indicate a very uniform ≈3L MoS<sub>2</sub> coverage on the n<sup>+</sup> 4H-SiC surface and ≈3.5L coverage on the n<sup>-</sup> 4H-SiC one.

In addition to the thickness uniformity, Raman mapping provided interesting information on the strain status of the as-grown MoS<sub>2</sub> films. In particular, the measured  $\omega_{E_{2g}}$  values are known to be very sensitive to the local biaxial strain ( $\epsilon$ ) induced by the interaction of MoS<sub>2</sub> membranes with the substrate, according to the relation:

$$\omega_{E_{2g}} = \omega_{E_{2g}^0} - 2\gamma_{E_{2g}} \omega_{E_{2g}^0} \epsilon \quad (1)$$

where  $\omega_{E_{2g}^0} = 382.9 \text{ cm}^{-1}$  is the E<sub>2g</sub> wavenumber for a suspended (i.e., unstrained) 3L MoS<sub>2</sub> membrane, while  $\gamma_{E_{2g}} = 0.39$  is the value of the Grüneisen parameter for 3L MoS<sub>2</sub>.<sup>[37]</sup> Figure S2a–c, Supporting Information shows the color maps and the histograms of the experimental  $\omega_{E_{2g}}$  values extracted from the arrays of Raman spectra on the MoS<sub>2</sub>/n<sup>-</sup>-SiC and MoS<sub>2</sub>/n<sup>+</sup>-SiC samples. From these distributions and according to Equation (1), we estimated similar compressive strain values of  $-0.34 \pm 0.02\%$  and  $-0.39 \pm 0.04\%$  for MoS<sub>2</sub> on the n<sup>-</sup>-type 4H-SiC and on n<sup>+</sup>-4H-SiC, respectively.

The position of the A<sub>1g</sub> peak is known to be sensitive to the interaction of the MoS<sub>2</sub> membrane with the substrate, specifically to the doping induced by charge transfer phenomena.<sup>[38]</sup> Figure S2d–f, Supporting Information shows the color maps and the histograms of the A<sub>1g</sub> wavenumbers obtained from arrays of 144 Raman spectra collected on 10 μm × 10 μm areas of the MoS<sub>2</sub>/n<sup>-</sup>-SiC and MoS<sub>2</sub>/n<sup>+</sup>-SiC samples. The very narrow distributions of the A<sub>1g</sub> wavenumbers indicate very uniform doping of MoS<sub>2</sub> membranes.

The structural properties of the MoS<sub>2</sub> heterojunctions with the 4°-off-axis 4H-SiC (0001) crystals have been further investigated by TEM analyses on cross-sectioned samples. Figure 2a,b are two representative high-resolution TEM images for PLD-grown MoS<sub>2</sub> on the unimplanted n<sup>-</sup> 4H-SiC epitaxy and on the n<sup>+</sup>-implanted 4H-SiC. In both cases, the MoS<sub>2</sub> films exhibit a uniform thickness and follow in a conformal way the characteristic steps of 4H-SiC surface due to the wafer 4°-off miscut angle. Looking more in detail at the number of MoS<sub>2</sub> layers, the presence of 3L–4L regions can be observed on the n<sup>-</sup> 4H-SiC sample (Figure 2a), whereas a more uniform 3L thickness is evident for the n<sup>+</sup> doped 4H-SiC surface, consistently with the results of Raman statistics. The presence of a very thin (≈1.4–1.5 nm) amorphous film at the interface between MoS<sub>2</sub> and SiC is also observed in the two samples. EDS chemical mapping, reported in Figure S3, Supporting Information, indicated that its composition is SiO<sub>2</sub>. Furthermore, the two TEM analyses in Figure 2a,b confirm a very good crystalline quality of 4H-SiC in the near interface region, even in the case of the n<sup>+</sup>-implanted sample. This is due to the lower phosphorus concentration (≈10<sup>19</sup> cm<sup>-3</sup>) in the near surface region of the implanted profile (see the SIMS in Figure S1, Supporting Information). On the other hand, the presence of implant-related defects in the 4H-SiC lattice at higher depths (from ≈90 to ≈170 nm), implanted with a P concentration of 10<sup>20</sup> cm<sup>-3</sup> can be observed in low magnification TEM analyses, shown in Figure S4, Supporting information. As it will be evident in the following, a comparable crystalline quality of 4H-SiC in the

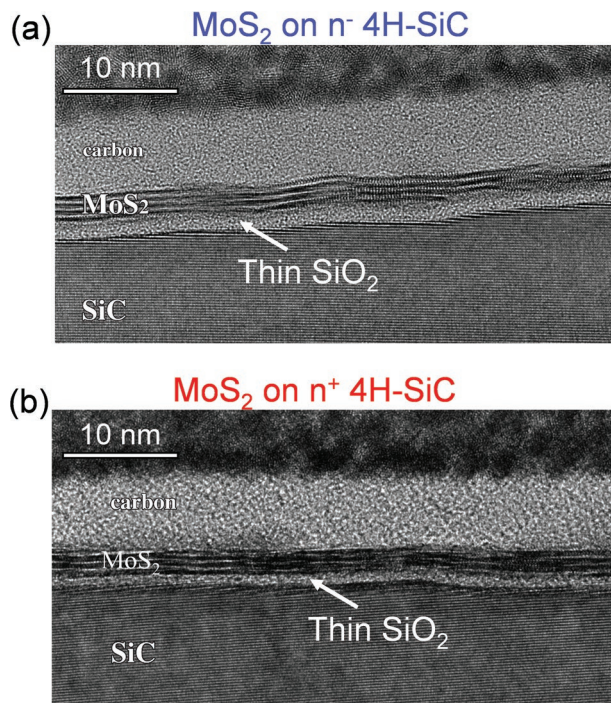


**Figure 2.** Cross-sectional high-resolution TEM images of MoS<sub>2</sub> on a) n<sup>-</sup> 4H-SiC and on b) n<sup>+</sup> implanted 4H-SiC.

near interface region is important for the interpretation of electrical transport properties of MoS<sub>2</sub>/SiC heterojunctions.

After this preliminary structural characterization, the current injection at the heterojunctions between the ultra-thin MoS<sub>2</sub> films and 4H-SiC with different surface doping has been investigated by current-voltage characterization of vertical diode structures, schematically illustrated in the inserts of Figure 3a,b. Two typical current density (*J*) versus bias characteristics measured at room temperature (*T* = 300 K) on the two samples are reported in Figure 3a,b. The MoS<sub>2</sub> junction with the moderately n-doped 4H-SiC (Figure 3a) exhibits an excellent rectifying behavior, with extremely low current density under reverse bias polarization ( $J_{\text{rev}} \approx 7.5 \times 10^{-8} \text{ A cm}^{-2}$  at -10 V), the exponential growth of the *J*-*V* characteristic under forward polarization ( $J_{\text{fw}} \approx 20 \text{ A cm}^{-2}$  at +3 V, limited by series resistance) and a resulting rectification ratio  $I_{\text{fw}}/I_{\text{rev}} \approx 10^8$ . On the other hand, a strongly enhanced current injection across the junction is observed for MoS<sub>2</sub> thin films grown on the degenerately n<sup>+</sup> doped 4H-SiC surface (Figure 3b), thus demonstrating the possibility of tailoring the vertical electronic transport by ion-implantation doping of the wide bandgap semiconductor. It is worth mentioning that the electrical characterization of Ni contacts on n<sup>-</sup> 4H-SiC and on n<sup>+</sup> 4H-SiC (implanted under identical conditions to those used in the present work) have been reported by Vivona et al.,<sup>[35]</sup> showing similar qualitative behavior the *I*-*V* characteristics but different values of the ideality factors and barrier heights.

To get a deeper insight on the physical mechanisms ruling current injection at the two heterojunctions, we performed a temperature-dependent electrical characterization of the diodes. Figure 4a,b shows the forward bias characteristics on the two

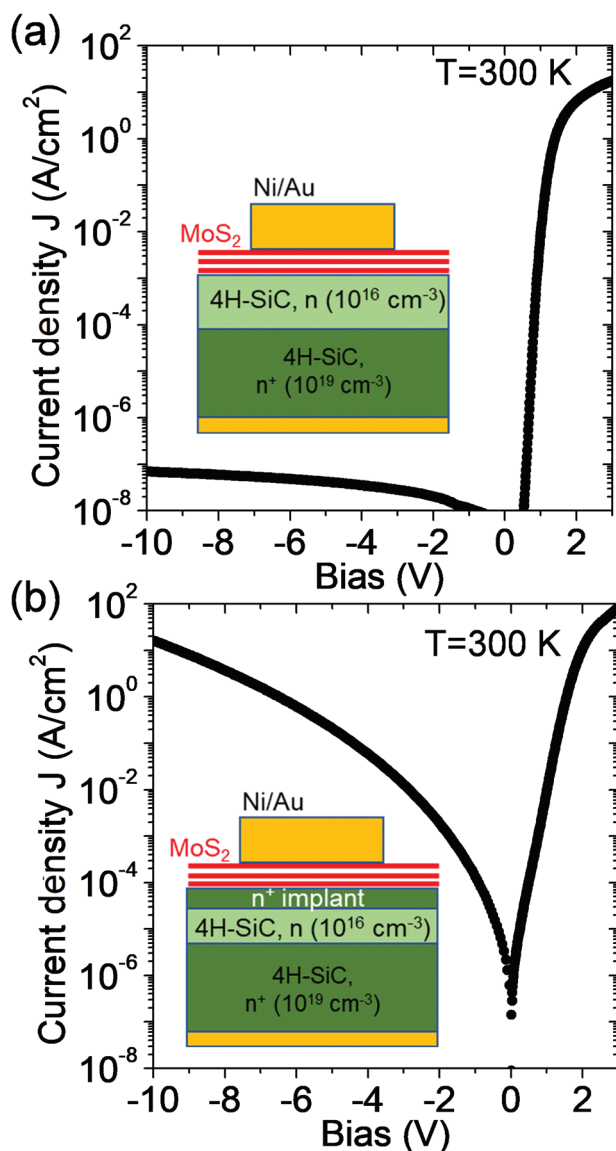


**Figure 3.** Current density-voltage characteristics of MoS<sub>2</sub> heterojunction diodes on a) n<sup>-</sup> - doped and b) n<sup>+</sup>-implanted 4H-SiC collected at room temperature ( $T = 300$  K). Schematic illustrations of the vertical diodes structure with Ni/Au top contact and backside contacts are reported in the insert of panels (a) and (b).

samples collected at different temperatures from 300 to 400 K. An increase of the current density  $J$  with  $T$  is observed in both cases, indicating the occurrence of temperature-activated electronic transport above/through an energy barrier, such as thermionic emission or thermionic field emission. The schematic band diagrams of the MoS<sub>2</sub>/SiO<sub>2</sub>/n<sup>-</sup>-SiC and MoS<sub>2</sub>/SiO<sub>2</sub>/n<sup>+</sup>-SiC heterojunctions are reported in the inserts of Figure 4a,b, respectively, where the band alignments have been estimated considering the literature values of energy bandgap and electron affinities for few-layers MoS<sub>2</sub>, SiO<sub>2</sub> and 4H-SiC.<sup>[39]</sup> Unintentional n-type doping of MoS<sub>2</sub> (as typically reported in the literature for MoS<sub>2</sub> produced by different methods) is considered for both heterojunctions, whereas n<sup>-</sup> and degenerate n<sup>+</sup> doping of 4H-SiC is accounted in the two cases. Due to the presence

of the ultra-thin SiO<sub>2</sub> interfacial layer, the  $J$ - $V$  characteristics of the junctions can be described, in a first approximation, with a modified thermionic emission equation:<sup>[40]</sup>

$$J = J_s e^{\frac{qV}{nk_B T}} \quad (2)$$

where  $q$  is the electron charge,  $k_B$  is the Boltzmann constant,  $n$  is the ideality factor, and the term  $J_s$  is expressed as:

$$J_s = A^* P_t T^2 e^{-\frac{q\Phi_B}{k_B T}} \quad (3)$$

being  $A^*$  the Richardson constant of 4H-SiC,<sup>[41]</sup>  $\Phi_B$  the heterojunction barrier between MoS<sub>2</sub> and 4H-SiC, and  $P_t$  the direct tunneling probability across the ultra-thin SiO<sub>2</sub> barrier. This latter term is expected to be temperature-independent and can be expressed as  $P_t = \exp\left[-\frac{4\pi\delta\sqrt{2m_{ox}\psi}}{h}\right]$ , being  $\psi \approx 2.7$  eV the

SiO<sub>2</sub>/4H-SiC conduction band discontinuity,<sup>[42]</sup>  $\delta \approx 1.4$  nm the thickness of the SiO<sub>2</sub> layer evaluated by TEM,  $m_{ox}$  the direct tunneling effective mass of SiO<sub>2</sub><sup>[43]</sup> and  $h$  the Planck's constant.

The current density term  $J_s$  and the ideality factor  $n$  for the two groups of  $J$ - $V$  characteristics in Figure 4a,b were obtained by fitting the linear region of each semilog curve with Equation (2) and taking the intercept and the slope, respectively. After evaluating the  $J_s$  terms at the different measurement temperatures  $T$ , the Arrhenius plots of the  $\ln[J_s/T^2]$  versus  $1000/T$  for the two heterojunction diodes have been built and reported in Figure 4c. According to Equation (3), the effective barrier height values for MoS<sub>2</sub> on n<sup>-</sup> 4H-SiC ( $\Phi_B = 1.04 \pm 0.09$  eV) and n<sup>+</sup> 4H-SiC ( $\Phi_B = 0.31 \pm 0.01$  eV) are obtained by the slopes of these plots. Furthermore, the dependence of the ideality factor  $n$  on the temperature  $T$  for the two heterojunction diodes is reported in Figure 4d.

Noteworthy, the experimentally determined energy barrier  $\Phi_B = (1.04 \pm 0.09)$  eV for the MoS<sub>2</sub> diode on the 4H-SiC epitaxy is very close to the value of the MoS<sub>2</sub>/SiC conduction band discontinuity  $\Delta E_C = \chi_{\text{MoS}_2} - \chi_{\text{4H-SiC}} \approx 1\text{eV}$ , where  $\chi_{\text{MoS}_2}$  and  $\chi_{\text{4H-SiC}}$  are the literature values of the electron affinities of the two semiconductors.<sup>[38,44]</sup> Furthermore, as shown in Figure 4d this diode exhibits an ideality factor  $n \approx 1.25$ , nearly independent on the measuring temperature  $T$ . According to the classical Card & Rhoderick model for metal-insulator-semiconductor tunnel junctions,<sup>[45]</sup> the slight departure of  $n$  from unity can be ascribed to the presence of traps states located at the interface between the thin SiO<sub>2</sub> layer and 4H-SiC, as expressed in the following equation:

$$n = 1 + \frac{qD_{it}\delta}{\epsilon_0\epsilon_{ox}} \quad (4)$$

where  $\epsilon_0$  is the vacuum dielectric constant,  $\epsilon_{ox} = 3.9$  the SiO<sub>2</sub> relative permittivity,  $\delta \approx 1.4$  nm the SiO<sub>2</sub> thickness, and  $D_{it}$  the interface traps density. By fitting the  $T$ -independent  $n$  behavior in Figure 4d with Equation (4), a  $D_{it} \approx 4 \times 10^{12} \text{ cm}^{-2} \text{ eV}^{-1}$  has been evaluated, which can be associated to carbon residues present in the nanometer SiO<sub>2</sub> film due to 4H-SiC oxidation.

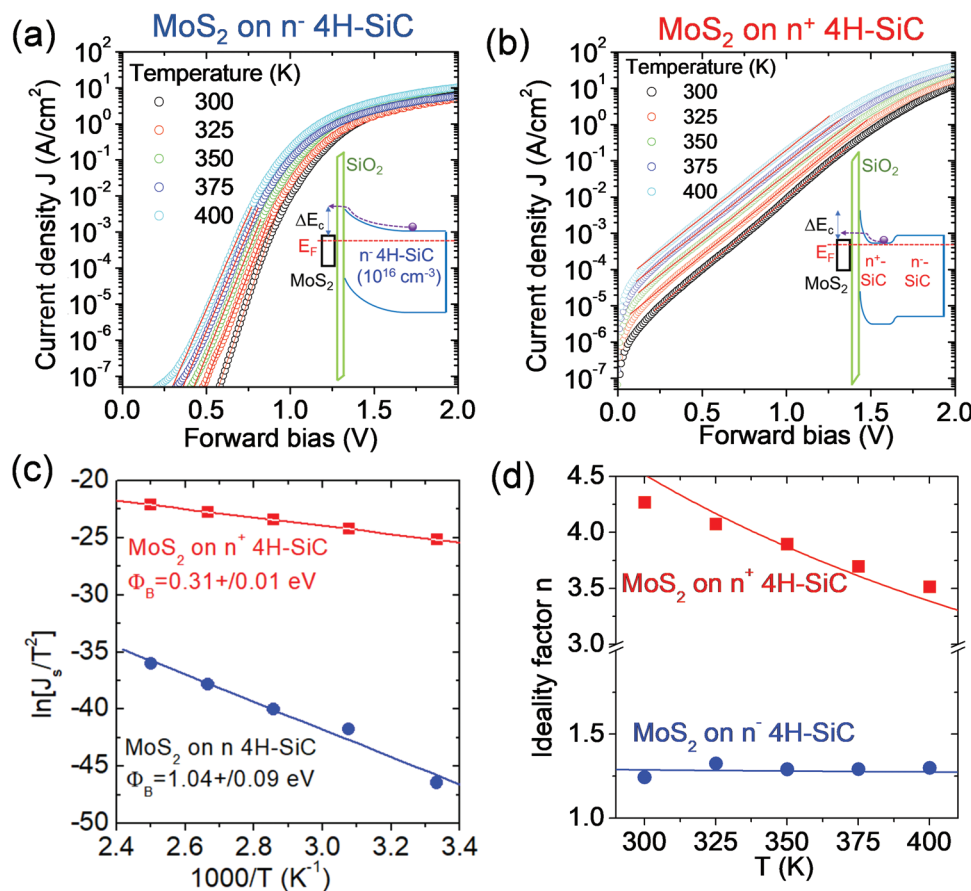


**Figure 4.** Forward bias current density–voltage ( $J$ – $V$ ) characteristics at different temperatures (from 300 to 400 K) for the MoS<sub>2</sub> diodes on n<sup>-</sup>4H-SiC (a) and on n<sup>+</sup> implanted 4H-SiC (b). The open circles represent the experimental data, whereas the red lines are the fits of the linear regions of the semilog  $J$ – $V$  curves. c) Arrhenius plots of  $\ln[J_s/T^2]$  versus  $1000/T$  for the two diodes and evaluation of the effective heterojunctions barrier heights from the slopes of the linear fits. d) Ideality factor  $n$  versus the measurement temperature for the two heterojunctions. The blue line is the fit of the  $T$ -independent  $n$ -values for the MoS<sub>2</sub>/SiO<sub>2</sub>/n<sup>-</sup>4H-SiC junction using the Card&Rhoderick model, whereas the red line is the fit of the  $n$  dependence on  $T$  considering the TFE model. The schematic band diagrams of the two MoS<sub>2</sub>/SiO<sub>2</sub>/SiC heterojunctions with an ultra-thin SiO<sub>2</sub> tunneling barrier are reported in the inserts of (a) and (b), with the illustration of the different current injection mechanisms deduced from the temperature-dependent electrical characterization.

The ideality factor close to unity and the good matching of the experimental barrier height  $\Phi_B$  with the MoS<sub>2</sub>/SiC conduction band discontinuity  $\Delta E_c$  confirms that thermionic emission above the barrier is the dominant current injection mechanism in MoS<sub>2</sub> diodes on n<sup>-</sup> 4H-SiC, as schematically illustrated in the insert of Figure 4a. On the other hand, the results in Figure 4d, e show that, for MoS<sub>2</sub> diodes on n<sup>+</sup> 4H-SiC, the evaluated effective barrier height ( $\Phi_B = 0.31 \pm 0.01$  eV) is much lower than  $\Delta E_c$ , while the ideality factor  $n$  strongly deviates from unity with a significant temperature dependence. The reduced effective barrier height indicates the tunneling of thermally excited electrons through the ultrathin depletion region of n<sup>+</sup>-doped 4H-SiC (as schematically depicted in the insert of Figure 4b), i.e., the occurrence of a thermionic field emission (TFE) mechanism. This mechanism is further supported by the temperature dependence of  $n$ . In fact, the current-voltage curves in the TFE processes can be expressed as:

$$J_{\text{TFE}} = J_{s,\text{TFE}} e^{\frac{qV}{E_0}} \quad (5)$$

where the voltage dependence is formally identical to the one for TE (Equation (1)), by expressing the characteristic energy  $E_0$  as  $E_0 = nk_B T/q$ . From this analogy, the temperature dependence of the ideality factor determined in Figure 4d can be described as<sup>[46]</sup>:

$$n = \frac{qE_0}{k_B T} = \frac{qE_{00}}{k_B T} \coth\left(\frac{qE_{00}}{k_B T}\right) \quad (6)$$

where the energy  $E_{00}$  depends on the surface donors concentration  $N_D$  of n<sup>+</sup> doped 4H-SiC as<sup>[35,45]</sup>:

$$E_{00} = \frac{h}{\pi} \sqrt{\frac{N_D}{m_{\text{eff,SiC}} \epsilon_0 \epsilon_{\text{SiC}}}} \quad (7)$$

being  $m_{\text{eff,SiC}} = 0.42 m_0$  the effective mass and  $\epsilon_{\text{SiC}} = 9.6$  the relative permittivity of 4H-SiC, respectively. By fitting the temperature dependence of  $n$  on  $T$  for MoS<sub>2</sub> diodes on n<sup>+</sup>-SiC with Equations (6)–(7), as shown in Figure 4d, a value of  $N_D \approx 1 \times 10^{19} \text{ cm}^{-3}$  is obtained. This is consistent with the active donors concentration in the surface region of implanted



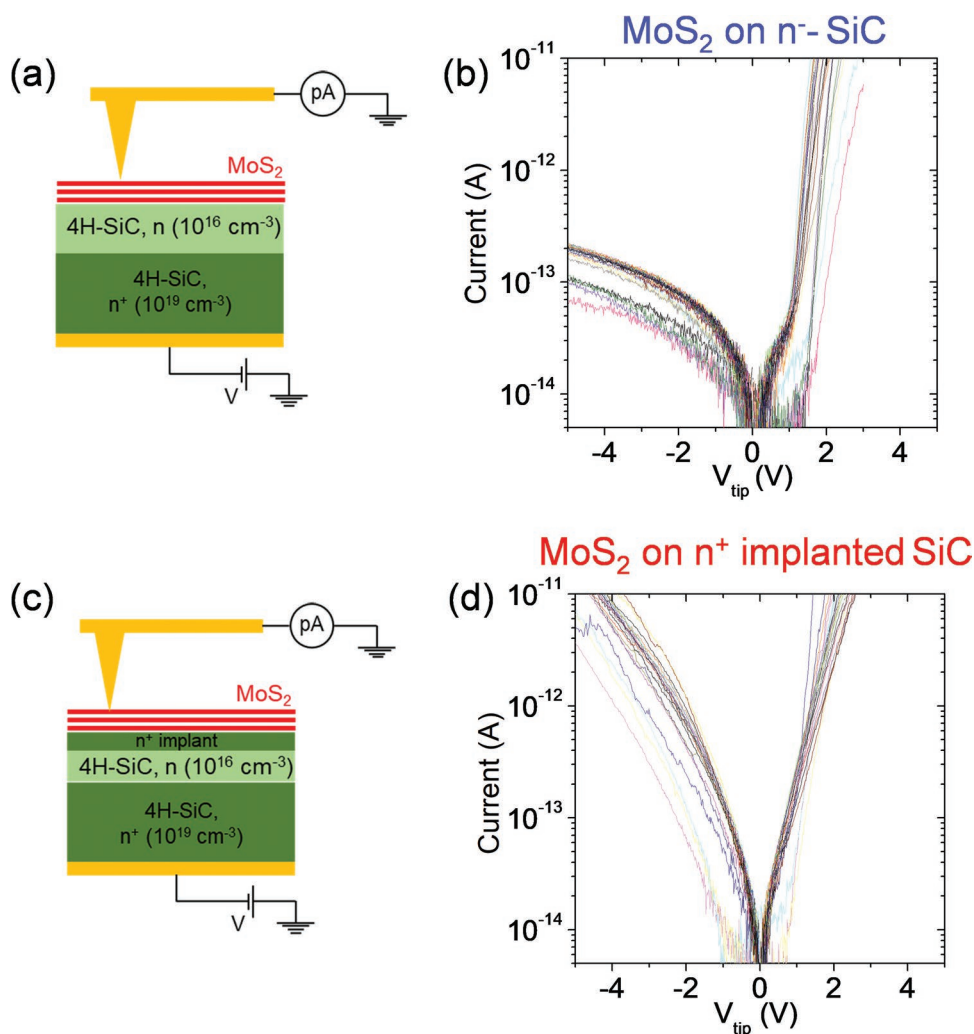


**Figure 5.** Schematic illustrations of the C-AFM setup for nanoscale resolution  $I$ - $V$  characterization and current mapping on MoS<sub>2</sub> heterojunctions with n<sup>-</sup> (a) and n<sup>+</sup>-implanted 4H-SiC (c). Local  $I$ - $V_{\text{tip}}$  characteristics collected on arrays of  $5 \times 5$  tip positions on MoS<sub>2</sub> on n<sup>-</sup>-SiC (b) and MoS<sub>2</sub> on n<sup>+</sup>-SiC (d).

4H-SiC, as illustrated in the profiles reported in Figure S1, Supporting Information. Furthermore, the high crystalline quality of the near-surface region of n<sup>+</sup>-implanted 4H-SiC, demonstrated by TEM analyses in Figure 2b, allows to exclude other transport mechanisms, such as tunneling mediated by implant-related defects in the n<sup>+</sup>-SiC depletion region.

The above-discussed temperature-dependent electrical analyses provide information on the average current injection behavior over the areas of macroscopic contacts (with 100  $\mu\text{m}$  radius). However, probing the local homogeneity of current transport down to nanometer scale is crucial, both to get a deeper insight on the electrical quality of the PLD-grown MoS<sub>2</sub> on 4H-SiC and in the perspective of realizing scaled or nanostructured devices. To this aim, local current-voltage ( $I$ - $V$ ) measurements and current mapping have been carried out directly on the as-deposited few-layer MoS<sub>2</sub> on n<sup>-</sup> and n<sup>+</sup>-doped 4H-SiC, using a Pt-coated Si tip as a nanoscale electrical contact, as schematically depicted in Figure 5a,c. Two representative sets of  $I$ - $V_{\text{tip}}$  curves collected by displacing the tip over two arrays of  $5 \times 5$  positions (with 1  $\mu\text{m}$  spacing) on the surface of

the two samples are reported in Figure 5b,d, respectively. All the local  $I$ - $V$  characteristics for MoS<sub>2</sub> on n<sup>-</sup>-4H-SiC exhibit a strongly rectifying behavior, whereas a significantly enhanced conduction under negative polarization is observed for MoS<sub>2</sub> on n<sup>+</sup>-implanted 4H-SiC.

The local barrier heights for the MoS<sub>2</sub>/SiC heterojunctions have been evaluated from the forward bias  $I$ - $V_{\text{tip}}$  collected by C-AFM, by properly adapting the thermionic emission model (Equations (2) and (3)) to the nanoscale system. Figure 6a schematically illustrates the Pt tip/MoS<sub>2</sub>/SiC heterojunction and the equivalent circuit, consisting in the series combination of different contributions, i.e., the tip resistance ( $R_{\text{tip}}$ ), the Pt/MoS<sub>2</sub> nano-contact resistance ( $R_{\text{C,nano}}$ ), the MoS<sub>2</sub>/SiC diode, the spreading resistance ( $R_{\text{spr}}$ ) of the locally injected current in the SiC bulk crystal, the drift resistance ( $R_{\text{d}}$ ) of bulk SiC and the macroscopic back-contact resistance ( $R_{\text{C,macro}}$ ). In particular, the  $R_{\text{tip}}$ ,  $R_{\text{d}}$  and  $R_{\text{C,macro}}$  are constant terms independent of the tip position, whereas  $R_{\text{C,nano}}$  depends on the local electrical properties of MoS<sub>2</sub> (i.e., the Pt/MoS<sub>2</sub> Schottky barrier and MoS<sub>2</sub> doping) and  $R_{\text{spr}}$  on the local resistivity of 4H-SiC.

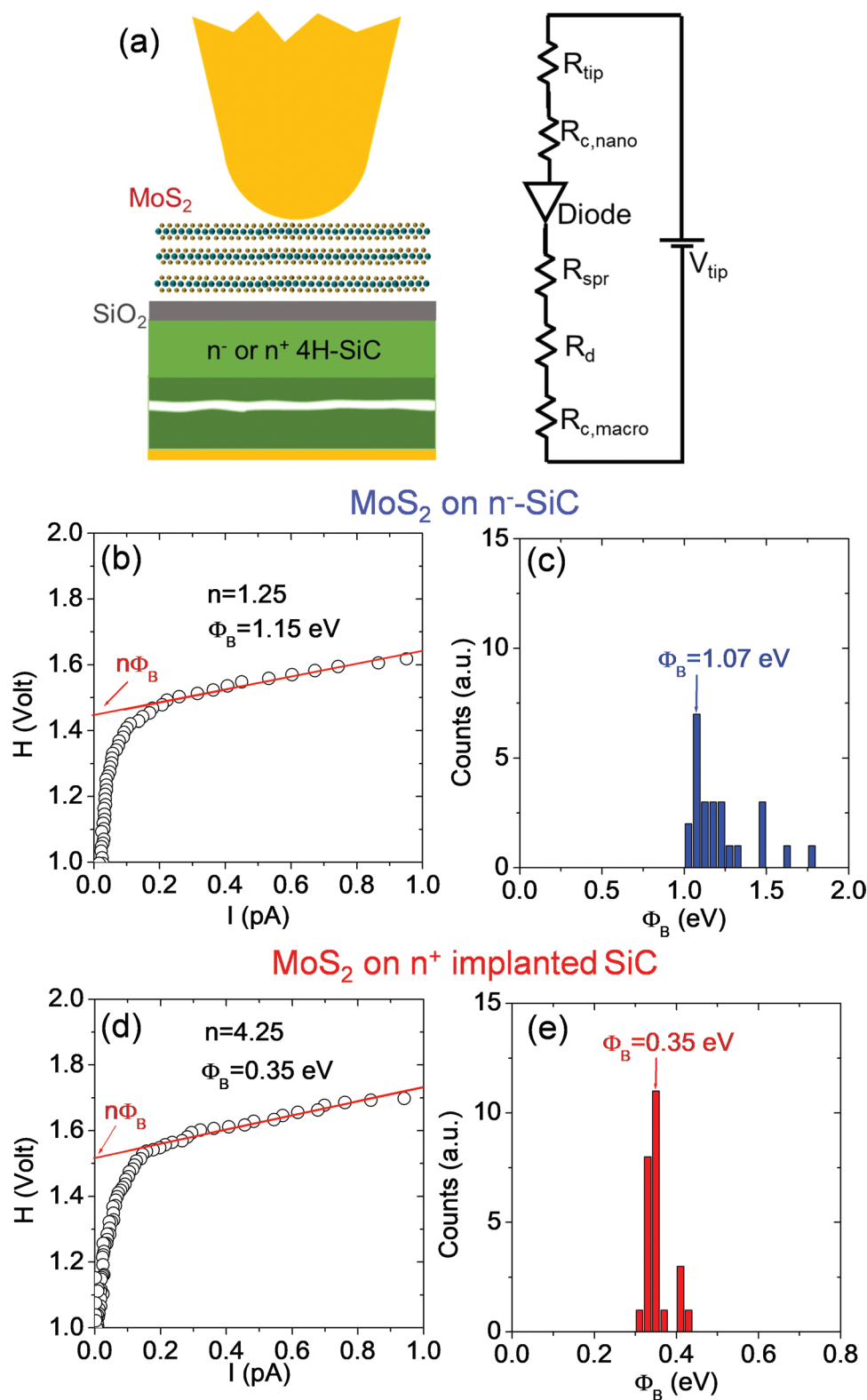


**Figure 6.** a) Schematic illustration of the nanoscale Pt tip contact with the MoS<sub>2</sub>/SiC heterojunctions and its equivalent circuit. H-I plots for single tip positions on MoS<sub>2</sub>/n<sup>-</sup>-SiC (b) and MoS<sub>2</sub>/n<sup>+</sup>-SiC (d), and the evaluation of the local barrier height values  $\Phi_B$ . Histograms of the local  $\Phi_B$  values obtained from H-I plots on arrays of 5 × 5 tip positions on MoS<sub>2</sub> on n<sup>-</sup>-SiC (c) and MoS<sub>2</sub> on n<sup>+</sup>-SiC (e).



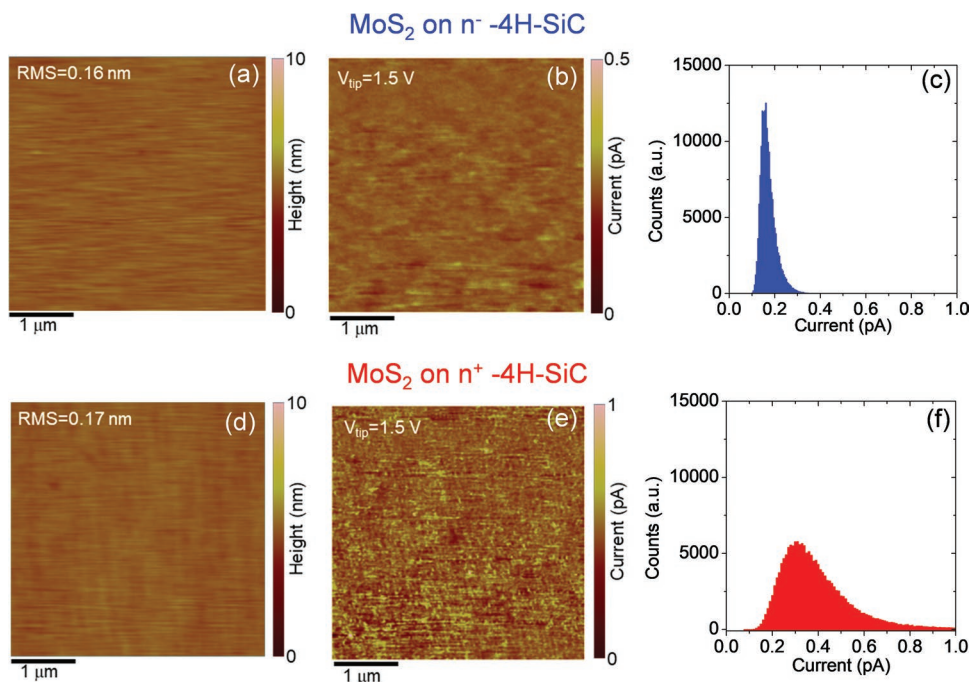


**Figure 7.** Surface morphology (a) and corresponding current map (b) obtained scanning the Pt tip on MoS<sub>2</sub> on n<sup>-</sup> 4H-SiC, while applying a bias V<sub>tip</sub> = 1.5 V with respect to the sample backside. Topography (d) and current map (e) collected under the same conditions for MoS<sub>2</sub> on n<sup>+</sup> 4H-SiC. c,f) Histograms of the current values extracted from the two current maps.

Due to the nanoscale tip contact size, the series resistance term  $R \approx R_{C,nano} + R_{spr}$  significantly affects the  $I-V_{tip}$  characteristics measured by C-AFM measured current. Hence, to account for this resistive term, the Equations. (2) and (3) have been modified as follows:

$$I = A_{tip} A^* P_t T^2 e^{-\frac{q\Phi_B}{k_B T}} e^{-\frac{q(V_{tip}-IR)}{nk_B T}} \quad (8)$$

where  $A_{tip} = \pi r_{tip}^2$  is the tip contact area, with  $r_{tip} \approx 5$  nm.

To evaluate the local barrier height value, Equation (8) has been linearized and arranged as:

$$H = n\Phi_B + IR \quad (9)$$

where the H function is defined as<sup>[47]</sup>:

$$H = V_{tip} - \frac{nk_B T}{q} \ln \left( \frac{I}{A_{tip} A^* P_t T^2} \right) \quad (10)$$

Figure 6b,d shows two H-I plots obtained from local  $I-V$  curves measured by the C-AFM tip on the MoS<sub>2</sub>/n<sup>-</sup> SiC (b) and MoS<sub>2</sub>/n<sup>+</sup> SiC (d) heterojunctions, respectively. Here, the ideality factor values ( $n = 1.25$  and  $n = 4.25$ ) extracted from macroscopic  $I-V$  measurements at 300 K (Figure 4d) have been used for the two samples. In Figure 6b,d, the local barrier height values ( $\Phi_B = 1.15$  eV and  $\Phi_B = 0.35$  eV for the MoS<sub>2</sub>/n<sup>-</sup> SiC and the MoS<sub>2</sub>/n<sup>+</sup> SiC junctions, respectively) were obtained according to Equation (9) by the intercept of the linear fits of the  $H-I$  curves on the vertical axis. Furthermore, the slopes of the fits

indicate similar values of the local series resistance ( $R \approx 200$  G $\Omega$ ) for the two samples.

Finally, Figure 6c,e shows the histograms of the local  $\Phi_B$  values obtained from  $H-I$  plots on arrays of  $5 \times 5$  tip positions on MoS<sub>2</sub> on n<sup>-</sup> SiC and MoS<sub>2</sub> on n<sup>+</sup> SiC, respectively. The peak values of these distributions ( $\Phi_B = 1.07$  eV and  $\Phi_B = 0.35$  eV) are in good agreement with the barrier height values obtained from temperature-dependent  $I-V$  analyses on macroscopic diodes (Figure 4c).

Besides local  $I-V$  characteristics, current mapping has been carried out using C-AFM, by scanning the metal tip on MoS<sub>2</sub> surface, while applying a dc bias with respect to the back contact. Figure 7a,b shows the surface morphology and corresponding current map obtained by scanning the Pt tip on the MoS<sub>2</sub>/n<sup>-</sup> SiC sample, while applying a positive bias ( $V_{tip} = 1.5$  V) with respect to the sample backside. The topography and current map collected under the same conditions for the MoS<sub>2</sub> on n<sup>+</sup> SiC are reported in Figure 7d,e. Furthermore, the histograms of the current values extracted from the two current maps are reported in Figure 7c,f. While similar and low surface roughness (RMS = 0.16 and 0.17 nm) is measured for both samples, MoS<sub>2</sub> on n<sup>-</sup> 4H-SiC exhibits a more uniform injected current distribution as compared to MoS<sub>2</sub> on n<sup>+</sup> 4H-SiC, as clearly demonstrated by the different shapes of the two histograms. In fact, for the first sample (Figure 7c) the histogram is more symmetric, with the peak at lower current and a short tail at higher current values. On the other hand, the histogram for the second sample exhibits the peak at a higher current and is much broader, with a longer tail at high current values. This tail is associated with the high current spots visible in the current map. These differences in the current distributions cannot be due to a different quality (e.g., defects

density) of the MoS<sub>2</sub> layers, since they have been grown under identical PLD conditions on the differently doped 4H-SiC samples. On the other hand, these can be explained by the different local barrier height distributions reported in Figure 6c,e. In fact, the higher values of  $\Phi_B$  for the MoS<sub>2</sub>/n<sup>-</sup>-SiC heterojunction gives rise to lower injected current by thermionic emission above the barrier. On the other hand, in the case of MoS<sub>2</sub> on n<sup>+</sup>-implanted SiC, the lower values of  $\Phi_B$  and the reduced SiC depletion region give rise to larger injected current by a thermionic-field-emission mechanism. Furthermore, the nanoscale variations of the barrier height (Figure 6e) and of the SiC depletion region thickness can give rise to the significant local variation of tunneling current, i.e., to the high current spots in the current map (Figure 7e).

#### 4. Conclusions

In conclusion, highly uniform MoS<sub>2</sub> films have been obtained by PLD on n<sup>-</sup>- and on n<sup>+</sup>-implanted 4H-SiC. Raman mapping with large statistics revealed an excellent thickness uniformity ( $\approx 3\text{L MoS}_2$ ) and low compressive strain (0.34–0.39%) of the PLD-grown films. Atomic resolution TEM analyses showed highly conformal coverage of MoS<sub>2</sub> on the 4<sup>o</sup>-off SiC surface, with the presence of an ultra-thin uniform SiO<sub>2</sub> layer at the interface, and an excellent crystallinity of near interface 4H-SiC, even for n<sup>+</sup>-implanted SiC. Current–voltage (*I*–*V*) characterizations on macroscopic diodes with patterned metal contacts and by nanoscale C-AFM measurements demonstrated a wide tunability of current injection at the hetero-interfaces by the near-surface doping of SiC, showing highly rectifying behavior on n<sup>-</sup> 4H-SiC and strongly enhanced reverse current on n<sup>+</sup>-implanted 4H-SiC. Finally, the mechanisms of current transport in these heterojunctions have been deeply investigated by temperature-dependent forward *I*–*V* characterizations, combined to nanoscale resolution C-AFM current mapping. Thermionic emission was shown to rule electron injection in MoS<sub>2</sub> on n<sup>-</sup> 4H-SiC, with an effective barrier  $\Phi_B = (1.04 \pm 0.09)$  eV, corresponding to the MoS<sub>2</sub>/SiC conduction band discontinuity, and temperature independent ideality factor ( $n \approx 1.25$ ) slightly departing from unity, due to a low density of interface traps between the ultra-thin SiO<sub>2</sub> and SiC. On the other hand, the significantly lower effective barrier  $\Phi_B = (0.31 \pm 0.01)$  eV and a temperature-dependent ideality factor *n* was explained by a thermionic-field-emission mechanism, with tunneling through the thin depletion region of n<sup>+</sup>-implanted 4H-SiC. The wide tunability of electronic transport in MoS<sub>2</sub>/SiC heterojunctions by SiC doping can be exploited in advanced or novel electronic device structures for energy efficient and fast switching applications.

#### Supporting Information

Supporting Information is available from the Wiley Online Library or from the author.

#### Acknowledgements

S. Di Franco (CNR-IMM, Catania) was acknowledged for the expert technical assistance with sample preparation. M. Vivona and

R. Lo Nigro (CNR-IMM, Catania), F. M. Gelardi (Univ. of Palermo), Y. Cordier, A. Michon and M. Al Khaloui (CNRS-CRHEA, France) are acknowledged for useful discussions. This work was funded, in part, by MUR in the framework of the FlagERA-JTC 2019 project ETMOS. Funding from CNR/SAS bilateral project PULSE and from CNR/HAS bilateral project GHOST-II for traveling is acknowledged. B.P. and A.K. acknowledged funding from the national projects TKP2021-NKTA-05 and NKFIH K\_134 258. Part of the experiments was carried out using the facilities of the Italian Infrastructure Beyond Nano.

Open Access Funding provided by Consiglio Nazionale delle Ricerche within the CRUI-CARE Agreement.

#### Conflict of Interest

The authors declare no conflict of interest.

#### Data Availability Statement

The data that support the findings of this study are available from the corresponding author upon reasonable request.

#### Keywords

conductive atomic force microscopy, heterojunction diodes, MoS<sub>2</sub>, pulsed laser deposition, silicon carbide

Received: July 8, 2022  
Revised: August 20, 2022  
Published online: October 4, 2022

- [1] S. Manzeli, D. Ovchinnikov, D. Pasquier, O. V. Yazyev, A. Kis, *Nat. Rev. Mater.* **2017**, *2*, 17033.
- [2] K. S. Novoselov, O. A. Mishchenko, O. A. Carvalho, A. H. Castro Neto, *Science* **2016**, *353*, aac9439.
- [3] F. Giannazzo, G. Greco, F. Roccaforte, S. S. Sonde, *Crystals* **2018**, *8*, 70.
- [4] D. Jariwala, T. J. Marks, M. C. Hersam, *Nat. Mater.* **2017**, *16*, 170.
- [5] P. Wang, C. Jia, Y. Huang, X. Duan, *Matter* **2021**, *4*, 552.
- [6] C.-Y. Huang, C. Chang, G.-Z. Lu, W.-C. Huang, C.-S. Huang, M.-L. Chen, T.-N. Lin, J.-L. Shen, T.-Y. Lin, *Appl. Phys. Lett.* **2018**, *112*, 233106.
- [7] R. Zhuo, Y. Wang, D. Wu, Z. Lou, Z. Shi, T. Xu, Y. Tian, X. Li, *J. Mater. Chem. C* **2018**, *6*, 299.
- [8] Y. Wu, Z. Li, K.-W. Ang, Y. Jia, Z. Shi, Z. Huang, W. Yu, X. Sun, X. Liu, D. Li, *Photonics Res.* **2019**, *7*, 1127.
- [9] M. Moun, R. Singh, *J. Appl. Phys.* **2020**, *127*, 135702.
- [10] S. K. Jain, R. R. Kumar, N. Aggarwal, P. Vashishtha, L. Goswami, S. Kuriakose, A. Pandey, M. Bhaskaran, S. Walia, G. Gupta, *ACS Appl Electron Mater* **2020**, *2*, 710.
- [11] Y. Xiao, L. Min, X. Liu, W. Liu, U. Younis, T. Peng, X. Kang, X. Wu, S. Ding, D. W. Zhang, *Nanophotonics* **2020**, *9*, 3035.
- [12] E. W. Lee, II, C. H. Lee, P. K. Paul, L. Ma, W. D. McCulloch, S. Krishnamoorthy, Y. Wu, A. R. Arehart, S. Rajan, *Appl. Phys. Lett.* **2015**, *107*, 103505.
- [13] S. Krishnamoorthy, E. W. Lee, C. H. Lee, Y. W. Zhang, W. D. McCulloch, J. M. Johnson, J. Hwang, Y. Y. Wu, S. Rajan, *Appl. Phys. Lett.* **2016**, *109*, 183505.
- [14] D. Ruzmetov, K. Zhang, G. Stan, B. Kalanyan, G. R. Bhimanapati, S. M. Eichfeld, R. A. Burke, P. B. Shah, T. P. O'Regan, F. J. Crowne, A. G. Birdwell, J. A. Robinson, A. V. Davydov, T. G. Ivanov, *ACS Nano* **2016**, *10*, 3580.

- [15] T. P. O'Regan, D. Ruzmetov, M. R. Neupane, R. A. Burke, A. A. Herzing, K. Zhang, A. G. Birdwell, D. E. Taylor, E. F. C. Byrd, S. D. Walck, A. V. Davydov, J. A. Robinson, T. G. Ivanov, *Appl. Phys. Lett.* **2017**, *111*, 051602.
- [16] D. Ruzmetov, M. R. Neupane, A. Herzing, T. P. O'Regan, A. Mazzoni, M. L. Chin, R. A. Burke, F. J. Crowne, A. Glen Birdwell, D. E. Taylor, A. Kolmakov, K. Zhang, J. A. Robinson, A. V. Davydov, T. G. Ivanov, *2D Mater.* **2018**, *5*, 045016.
- [17] E. W. Leell, L. Ma, D. N. Nath, C. H. Lee, A. Arehart, Y. Wu, S. Rajan, *Appl. Phys. Lett.* **2014**, *105*, 203504.
- [18] H. Jeong, S. Bang, H. M. Oh, H. J. Jeong, S.-J. An, G. H. Han, H. Kim, K. K. Kim, J. C. Park, Y. H. Lee, G. Lerondel, M. S. Jeong, *ACS Nano* **2015**, *9*, 10032.
- [19] P. Yan, Q. Tian, G. Yang, Y. Weng, Y. Zhang, J. Wang, F. Xie, N. Lu, *RSC Adv.* **2018**, *8*, 33193.
- [20] C. Liu, H. Huang, W. Choi, J. Kim, K. Jung, W. Sun, N. Tansu, W. Zhou, H. Kuo, X. Li, *ACS Appl Electron Mater* **2020**, *2*, 419.
- [21] C. R. Serrao, A. M. Diamond, S.-L. Hsu, L. You, S. Gadgil, J. Clarkson, C. Carraro, R. Maboudian, C. Hu, S. Salahuddin, *Appl. Phys. Lett.* **2015**, *106*, 052101.
- [22] M. Stockmeier, R. Müller, S. A. Sakwe, P. J. Wellmann, A. Magerl, *J Appl Phys* **2009**, *105*, 033511.
- [23] R. Murray, B. Evans, *J. Appl. Crystallogr.* **1979**, *12*, 312.
- [24] Z. Li, R. C. Bradt, *J. Appl. Phys.* **1986**, *60*, 612.
- [25] D. Wu, T. Min, J. Zhou, C. Li, G. Ma, G. Lu, M. Xia, Z. Gu, *Sci. Rep.* **2017**, *7*, 15166.
- [26] F. Lan, Z. Lai, Y. Xu, H. Cheng, Z. Wang, C. Qi, J. Chen, S. Zhang, *Sci. Rep.* **2016**, *6*, 31980.
- [27] J. Bradford, A. Zaganelli, D. Qi, N. Zebardastan, M. Shafei, J. MacLeod, N. Motta, *Appl. Surf. Sci.* **2021**, *552*, 149303.
- [28] F. Roccaforte, P. Fiorenza, G. Greco, R. Lo Nigro, F. Giannazzo, F. Iucolano, M. Saggio, *Microelectron. Eng.* **2018**, *187–188*, 66.
- [29] F. Giannazzo, S. E. Panasci, E. Schilirò, F. Roccaforte, A. Koos, M. Nemeth, B. Pécz, *Adv. Mater. Interfaces* **2022**, *9*, 2200915.
- [30] F. Giannazzo, G. Greco, E. Schilirò, R. Lo Nigro, I. Deretzis, A. La Magna, F. Roccaforte, F. Iucolano, S. Ravesi, E. Frayssinet, A. Michon, Y. Cordier, *ACS Appl Electron Mater* **2019**, *1*, 2342.
- [31] C. M. Torres, Y.-W. Lan, C. Zeng, J.-H. Chen, X. Kou, A. Navabi, J. Tang, M. Montazeri, J. R. Adleman, M. B. Lerner, Y.-L. Zhong, L.-J. Li, C.-D. Chen, K. L. Wang, *Nano Lett.* **2015**, *15*, 7905.
- [32] M. Lanza, *Conductive Atomic Force Microscopy: Applications in Nanomaterials*, Wiley-VCH Verlag, Weinheim, Germany **2017**.
- [33] F. Giannazzo, E. Schilirò, G. Greco, F. Roccaforte, *Nanomaterials* **2020**, *10*, 803.
- [34] M. Spera, G. Greco, A. Severino, M. Vivona, P. Fiorenza, F. Giannazzo, F. Roccaforte, *Appl. Phys. Lett.* **2020**, *117*, 013502.
- [35] M. Vivona, G. Greco, M. Spera, P. Fiorenza, F. Giannazzo, A. La Magna, F. Roccaforte, *J. Phys. D: Appl. Phys.* **2021**, *54*, 445107.
- [36] C. Lee, H. Yan, L. E. Brus, T. F. Heinz, J. Hone, S. Ryu, *ACS Nano* **2010**, *4*, 2695.
- [37] D. Lloyd, X. Liu, J. S. Christopher, L. Cantley, A. Wadehra, B. L. Kim, B. B. Goldberg, A. K. Swan, J. S. Bunch, *Nano Lett.* **2016**, *16*, 5836.
- [38] S. E. Panasci, E. Schilirò, F. Migliore, M. Cannas, F. M. Gelardi, F. Roccaforte, F. Giannazzo, S. Agnello, *Appl. Phys. Lett.* **2021**, *119*, 093103.
- [39] H. Lee, S. Deshmukh, J. Wen, V. Z. Costa, J. S. Schuder, M. Sanchez, A. S. Ichimura, E. Pop, B. Wang, A. K. M. Newaz, *ACS Appl. Mater. Interfaces* **2019**, *11*, 31543.
- [40] S. M. Sze, K. K. Ng, *Physics of Semiconductor Devices*, 3rd ed., John Wiley & Sons, Hoboken, New Jersey **2007**.
- [41] F. Roccaforte, F. La Via, V. Raineri, R. Pierobon, E. Zanoni, *J. Appl. Phys.* **2003**, *93*, 9137.
- [42] V. V. Afanasev, M. Bassler, G. Pensl, M. J. Schulz, E. Stein von Kamienski, *J. Appl. Phys.* **1996**, *79*, 3108.
- [43] M. Lenzlinger, E. H. Snow, *J. Appl. Phys.* **1969**, *40*, 278.
- [44] S. Y. Davydov, *Semiconductors* **2007**, *41*, 696.
- [45] H. C. Card, E. H. Rhoderick, *J. Phys. D: Appl. Phys.* **1971**, *4*, 1589.
- [46] G. Greco, P. Fiorenza, M. Spera, F. Giannazzo, F. Roccaforte, *J. Appl. Phys.* **2021**, *129*, 234501.
- [47] S. K. Cheung, N. W. Cheung, *Appl. Phys. Lett.* **1986**, *49*, 85.